Enhanced catalytic activity in Nb-doped TiO$_2$ for electrochemical oxygen reduction reaction

Muhammed Fasil Puthiyaparambath and Raghu Chatanathodi ●[*]

Department of Physics, National Institute of Technology Calicut, Kerala 673601, India

TiO$_2$ has wide applications in catalysis and photocatalysis and is an attractive alternative to Pt or Pt-based catalysts due to its abundance, low cost, and nontoxicity. However, it does not display any worthwhile catalytic activity as far as the oxygen reduction reaction (ORR) is concerned. Attempts have been made to improve the activity of TiO$_2$ by doping and creating defects on the surface. Nb-doped TiO$_2$ is experimentally found to have good conductivity and electrochemical activity for low-Nb concentrations. This paper presents a systematic modeling study of how Nb doping influences the ORR activity of anatase TiO$_2$ using plane-wave density-functional theory method. We elucidate the probable dopant sites, the effect of Nb doping on the oxygen binding capability at active sites, the favored reaction pathway, and the transition state. We find a remarkable enhancement in the capability of TiO$_2$ to catalyze ORR upon doping with Nb. We have also modeled the effect of solvation on the binding of oxygen and other reaction intermediates, using a model where water molecules are added as a monolayer over Nb-doped TiO$_2$. Solvation introduces additional hydrogen bonding, which improves the binding of intermediates to the active site and lowers activation barriers. Our model for ORR in Nb-doped TiO$_2$ agrees with recent experimental results on the same.

I. INTRODUCTION

Proton-exchange membrane fuel cells (PEMFCs) have gained significant research attention due to their high energy-conversion efficiency, high power output, absence of environmental pollution, and potential applications in powering transportation and portable electronic devices [1–3]. During the discharging process in PEMFCs, the oxygen reduction reaction (ORR) occurs at the cathode. However, the reaction is hindered by slow kinetics. An efficient catalyst is required for the ORR to occur at a reasonable rate. Pt and Pt-based materials have been widely employed as catalysts for the ORR [4–6]. Nevertheless, the high cost, low abundance, poor CO tolerance, and low durability of Pt hinder the large-scale deployment of fuel cells. Highly efficient cathodic catalysts are required to overcome these challenges [7]. Thus, developing nonprecious-metal based catalysts, such as transition-metal oxides (TMOs) [8], perovskites [9], carbon-based materials [10], and metal nitrides [11,12] for replacing Pt catalysts is a much-pursued research goal.

TMOs are potential candidates for ORR electrocatalysts by their variable oxidation state, corrosion resistance, and electronic conductivity [13–15]. Among these, TiO$_2$ is widely employed in catalysis and photocatalysis [16,17] due to its abundance, nontoxicity, and stability under various conditions. TiO$_2$ occurs in nature in two different structures, rutile and anatase. Rutile is the thermodynamically stable phase of TiO$_2$, while anatase is a technologically important metal oxide widely used in various catalytic applications

[18]. Unfortunately, in the case of ORR, anatase TiO$_2$ is inactive because its surface exhibits weak oxygen binding. This weak binding hinders the breaking of the O–O bond, which affects the overall progress of the ORR [19,20]. These limitations can be overcome by employing various strategies, such as metal doping, structural defects like oxygen vacancies, and promoting strong metal-support interactions. These strategies also trigger the electrical conductivity and increase the donor density, enhancing the overall catalytic performance.

Doping heterogeneous atoms is one of the straightforward ways to enhance the ORR activity of TiO$_2$. Previous reports suggest that molybdenum-doped TiO$_2$ with Pt support shows resistance against carbon and enhances its ORR activity [21]. Elezović *et al.* [22] suggested that doping TiO$_2$ with Ru in the presence of a Pt support resulted in enhanced catalytic activity compared to Pt/C. A novel Fe-doped TiO$_2$-based aerogel was developed, enhancing mass transfer and exposing more active sites as an ORR catalyst. The presence of oxygen vacancies and Fe doping in anatase increases the electrical conductivity by generating impurity-energy levels, thereby improving the kinetics of ORR [23]. Theoretical calculations performed on Zn-modified TiO$_2$ suggest a synergistic effect between surface H and subsurface Zn interstitial, favoring O$_2$ dissociation [24]. Liu and co-workers conducted density-functional theory (DFT) calculations and employed nudged elastic band (NEB) method to investigate O$_2$ adsorption on anatase TiO$_2$ (101) surfaces with subsurface Ti interstitials. Their results revealed that the presence of subsurface Ti significantly improved the O$_2$ dissociation, thereby enhancing the catalytic performance [25]. Deposition of noble metals such as Au or Pt on the TiO$_2$ surface enhances the ORR activity [20,26,27]. Li *et al.* [28] synthesized novel TiO$_2$ with

_____

[*]Corresponding author: raghuc@nitc.ac.in

oxygen vacancy-supported Pd nanoparticles, demonstrating superior ORR activity and methanol tolerance. DFT calculations reveal the electron transfer from defective TiO_2 to Pd, resulting in an electron-rich environment that enhances the ORR activity. However, due to the high cost of noble metals, these materials are not beneficial for large-scale applications.

Niobium-doped TiO_2 (abbreviated as $Nb-TiO_2$) is a promising catalyst due to its relatively high conductivity [29,30] and electrochemical stability. Arashi *et al.* [31] developed $Nb-TiO_2$ as an electrocatalyst for ORR and found that the optimal condition for ORR was achieved through H_2 treatment at a relatively high temperature. They observed a significant decrease in the ORR activity of $Nb-TiO_2$ after postcalcination, which may be due to the reduction in the conductivity and the removal of carbon residues. Chevallier and co-workers proposed an innovative method for synthesizing Nb-doped nanocrystalline TiO_2, which exhibits enhanced electrochemical properties. Despite the slightly lower mass activity obtained at 0.9 V vs reversible hydrogen electrode (RHE), $Nb-TiO_2$ shows the highest stability compared to other catalysts [32]. Another group synthesized $Nb-TiO_2$ nanofiber support for Pt using the electrospinning technique and found enhanced ORR activity and durability [33].

Furthermore, $Nb-TiO_2$ in the rutile phase with Pt support shows tenfold higher catalytic activity than Pt/C catalyst [34]. Alvar and co-workers pioneered the discovery of embedding carbon onto $Nb-TiO_2$ nanofibers and tested the ORR activity with and without Pt support. The experiments also revealed that $Nb-TiO_2$ with 10% Nb exhibited superior properties to those with 25% Nb. This is attributed to the higher concentration of Nb leading to the formation of oxide, while the lower concentration allows for the incorporation of Nb into the TiO_2 lattice [35]. Moreover, $Nb-TiO_2$ films' resistivity decreased with the increasing Nb concentration up to 6.4 at. % [36]. A later work by Lee *et al.* [37] systematically synthesized Nb-incorporated TiO_2 through hydrothermal processes. The x-ray-diffraction results showed a shift in the diffraction peak of anatase TiO_2 to a lower angle as the Nb content increased, indicating the exchange of the Ti atom with the Nb atom and a subsequent reduction in crystallinity.

Previous research [38–41] experimentally validated that the $Nb-TiO_2$ is ORR active. However, the exact pathway, possible doping sites/configurations, and the reaction mechanism remain unknown to the best of our knowledge. Thus, a fundamental, model-based understanding of the role of dopants in ORR catalyzed by $Nb-TiO_2$ is essential, as they can significantly alter the properties and performance of the catalyst. We have carried out our studies of $Nb-TiO_2$ in the low-dopant concentration regime, where experiments see enhancement of ORR activity. We have focused on the (101)-oriented anatase TiO_2 surface, which is the stable facet. Nb doping by substituting a Ti and occupation of interstitial sites are considered. The stability of the dopant, the resultant changes in the electronic structure of anatase TiO_2, site preference for oxygen and ORR intermediates adsorption, the preferred ORR pathway, and the effect of solvation on binding and activation barrier are investigated. The following section discusses our models and the details of computational methods. Further, we present our main results and discuss these.

II. COMPUTATIONAL METHODOLOGY

All calculations were performed using the Vienna *ab initio* Simulation Package (VASP) [42,43], with a spin-polarized first-principles approach. The Perdew-Burke-Ernzerhof exchange-correlation functional was employed with an energy cutoff of 540 eV for the plane-wave basis-set expansion [44]. The van der Waals interaction was included in all calculations through the semiempirical method of DFT-D2 proposed by Grimme [45,46]. The interaction between valence electrons and frozen cores was described by the projector augmented-wave method [47]. The generalized gradient approximation plus Hubbard U (GGA + U) method was used to calculate the electronic structure of anatase TiO_2 in order to reduce the underestimation of the band gap and guarantee a qualitative description of the electronic properties. The value of the Hubbard parameter was set to 4.2 eV for Ti 3d as suggested in other theoretical works [48,49]. The lattice parameter for the bulk anatase TiO_2 was obtained as $a = 3.824$ Å and $c = 9.576$ Å with GGA, and $a = 3.888$ Å and $c = 9.594$ Å with GGA + U, which are in agreement with the experimental values [50].

The anatase (001) facet has been reported to be the most active surface in catalytic processes, whereas the (101) facet is the most stable facet [51,52]. A 1×3 supercell of (101) anatase TiO_2 was modeled with three stoichiometric layers (108 atoms in total), of which the bottom layer was fixed to stimulate the bulk structure and the remaining layers were relaxed. The Brillouin zone was sampled using a $3 \times 3 \times 1$ Monkhorst-Pack grid [53]. During the structural optimization, the electronic energy was converged to 10^{-5} eV and the total energy to 10^{-4} eV. An 18-Å vacuum was added along the z direction of the simulation cell to minimize any interaction between periodic images.

The electronic structures of pristine and Nb-doped TiO_2 were calculated. The formation energy of the substitution-doped system is calculated by the formula

$$E_f = E_{tot} - E_{TiO_2} - \mu_{Nb} + \mu_{Ti},$$

where E_{tot} is the doped system energy, E_{TiO_2} is the pristine TiO_2 energy, $\mu_{Nb} = \mu_{NbO} - \mu_O$ and $\mu_{Ti} = \mu_{TiO2} - 2\mu_O$. The formation energy of the interstitial doped system is

$$E_f = E_{tot} - E_{TiO_2} - \mu_{Nb}.$$

The adsorption energies (E_{ads}) of various adsorbents on (101) anatase TiO_2 were calculated through

$$E_{ads} = E_{sys} - E_{surf} - E_X,$$

where E_{sys}, E_{surf}, and E_X are the total energies of adsorbed systems, the pristine or Nb-doped TiO_2, and the energy of an isolated adsorbate species, respectively. X indicates O_2, OOH, H, O, OH, H_2O, and HOOH. More negative adsorption energies indicate strong adsorption. The enthalpy of the reaction (ΔE) and the activation energy (E_a) for dissociation, protonation, and diffusion process were calculated using the climbing-image nudged elastic band (CI-NEB) method [54]. The initial and final states were constructed based on the adsorption of the chemical species on TiO_2. Bader charges [55,56] were calculated to determine the amount of charge
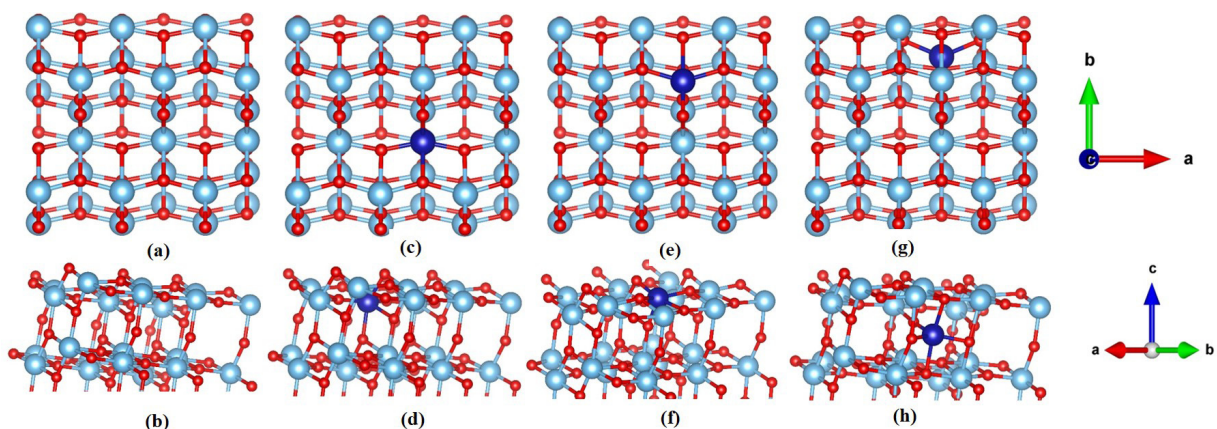
FIG. 1. Top and side view of fully relaxed TiO$_2$ slab (a, (b); Nb substituted at Ti$_{6c}$ site (c, (d); Nb substituted at Ti$_{5c}$ site (e), (f); and Nb at interstitial site (g), (h), where blue, violet, and red spheres represent Ti, Nb, and oxygen, respectively.

transfer for the optimized geometries of free O$_2$, Nb-doped TiO$_2$, and O$_2$-Nb-TiO$_2$.

III. RESULTS AND DISCUSSION

As stated previously, anatase TiO$_2$ does not show any significant ORR activity. Our study investigates the enhancement of ORR activity in Nb-doped anatase TiO$_2$. For this purpose, we have constructed a model of the anatase (101) surface and studied the substitution of Ti by Nb, its stability, and electronic structure changes due to doping. The adsorption of O$_2$ and ORR intermediates over Nb-TiO$_2$ was then investigated, with a detailed study of the reaction pathway and transition state.

A. Niobium-doped structures

The fully relaxed structure of pristine anatase (101) slab is shown in Figs. 1(a) and 1(b). The substitution of a single Ti atom by Nb can be done in two different ways: replacing a six-coordinated Ti (Ti$_{6c}$), or a five-coordinated Ti (Ti$_{5c}$). The relaxed structures after these substitutions are displayed in Figs. 1(c) and 1(d), and 1(e) and 1(f), respectively. It may be noted that Nb substituted at Ti$_{5c}$ is at the surface while at Ti$_{6c}$, it is subsurface. Figures 1(g) and 1(h) show doping at the interstitial site. Four distinct interstitial sites are available for doping. Following Liu *et al.* [24], the sites are named S1, S2, S3, and S4 (see Supplemental Material Fig. S1) [57]. S1 indicates that the Nb atom occupies a position along the surface between two two-coordinated oxygens (O$_{2c}$), while S2, S3, and S4 are subsurface sites.

Formation energy of doped structures is calculated as given in the previous section. All the considered doped systems have different formation energies. Amongst the substituted sites, we find that Nb substitution at Ti$_{6c}$ (−1.07 eV) has lower formation energy than at Ti$_{5c}$ (−0.77 eV) site. The formation energies for the interstitial doped configurations have been calculated and tabulated (see Supplemental Material Table S1) [57]. The results reveal that the S4 dopant site (3.45 eV) is relatively more stable than the others.

In order to understand more about the stability of the interstitial doping of TiO$_2$ with Nb, we have considered the

possibility of diffusion of the dopant from the surface to subsurface position. Using the CI-NEB method, the transformation from S1 to S4 is calculated to analyze the stabilities of S1, S2, S3, and S4. The results of these calculations are displayed in Fig. 2. Two metastable interstitials, S2 and S3, were identified during this transformation. Nb at S1 diffuses to S2 with a barrier of 0.47 eV, then to S3 with a barrier of 0.17 eV, and finally to S4 with a barrier of 0.46 eV. The maximum barrier is thus 0.47 eV from S1 to S4, while for the reverse diffusion from S4 to S1, it is greater than 0.90 eV. Therefore, we conclude that interstitial Nb could stably occur in the subsurface S4 site. Hereon, the term interstitial doping in this study will refer to only the stable S4 configuration.

It is also found that the computed adsorption energy of O$_2$ on Nb is maximum at the S1 site (−4.60 eV), and lower for all other interstitial sites. Correspondingly, the bond length of adsorbed O$_2$ is also very high at 1.48 Å, implying a very strong binding (see Supplemental Material Figs. S2 and S3)
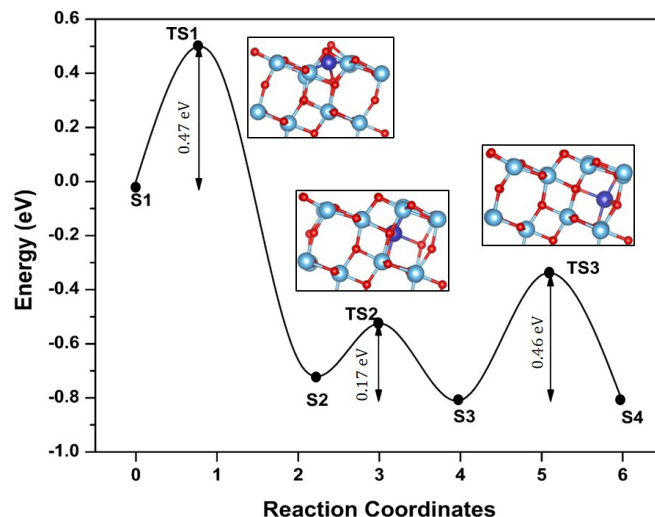

FIG. 2. Potential-energy profile for diffusion of doped Nb atom in interstitial site of pristine TiO$_2$ (101), where blue, violet, and red spheres represent Ti, Nb, and oxygen, respectively.

TABLE I. Structural parameters of Nb-doped TiO_2. All distances are in Å.

System	5c site (Å)			6c site (Å)		
	In plane		Out of plane	In plane		Out of plane
	x	y	z	x	y	z
Pristine TiO_2	1.99	1.84	1.80	1.95	2.09	1.88
Ti_{6c}	1.97	1.88	1.82	1.95	2.12	1.92
Ti_{5c}	1.99	1.85	1.81	1.93	2.20	2.00
Interstitial	1.99	1.89	1.92	1.95	2.23	1.84

[57]. These numbers help us to understand the reason for the formation of Nb oxide at high levels of Nb doping, leading to a loss of ORR efficiency, in the work of Alvar *et al.* [35]. At low doping levels, Nb would probably reach the available subsurface positions S4 and fill these up, while at high doping levels, a large number of interstitial Nb would be present on the surface, which would then readily bind oxygen to form oxide.

To further investigate the stability of Nb-doped TiO_2, *ab initio* molecular-dynamics (AIMD) simulations were performed with a 2000-fs time step for the Ti_{6c}, Ti_{5c}, and the interstitial doped structures with temperature, employing the Nosé-Hoover thermostat. From the time traces of the MD simulation and structures at 300 K, we observe that the total energy of the doped system has very marginal fluctuations at 300 K (see Supplemental Material Fig. S4) [57]. This tells us that the Nb-doped TiO_2 structures are stable at room temperature, without any distortions or bond breaks.

The TiO_6 octahedra is a key element of the TiO_2 structure, with the Ti–O bonds dividing into in-plane (*X-Y*) and out-of-plane (Z) directed bonds. In pristine TiO_2, the optimized in-plane Ti–O bond lengths are 1.99 and 1.84 Å, and out of plane is 1.80 Å for the Ti_{5c} site. For the Ti_{6c} site, it is 1.95 and 2.09 Å in plane and 1.88 Å out of plane. With doping of Nb, the bond lengths are changed with further distortion of the octahedra, as shown in Table I below. In the case of interstitial doped TiO_2, there is significant distortion due to the incorporation of Nb. Ti atom at the surface immediately above the interstitial site is pushed upwards by a distance of 0.12 Å from its initial position to accommodate the Nb atom because of the larger ionic radius of the Nb atom.

To reveal the influence of Nb doping on the electronic structure of (101) TiO_2 surface, the projected density of states (PDOS) of Ti_{6c}, Ti_{5c}, and interstitial doped Nb TiO_2 was calculated (Fig. 3) and compared with that of pristine TiO_2. In pristine TiO_2, the bottom of the conduction band is composed of Ti 3*d* states, while the top of the valence band is composed of O 2*p* states, as seen from Fig. 3(a). This description of TiO_2 is in good agreement with several previous descriptions, where the low-energy parts of the conduction band are deemed to be made of d_{xz}, d_{yz} (π^*), and d_{xy} states of Ti, while the d_{z^2} and $d_{x^2-y^2}$ form the higher-energy σ^* states. The edge of the valence band is made mainly out of nonbonding out-of-plane O p_π states and the π and σ states produced out of hybridization of O 2*p* with Ti 3*d*. For a more detailed description, the reader is referred to Peng *et al.* [58]. With
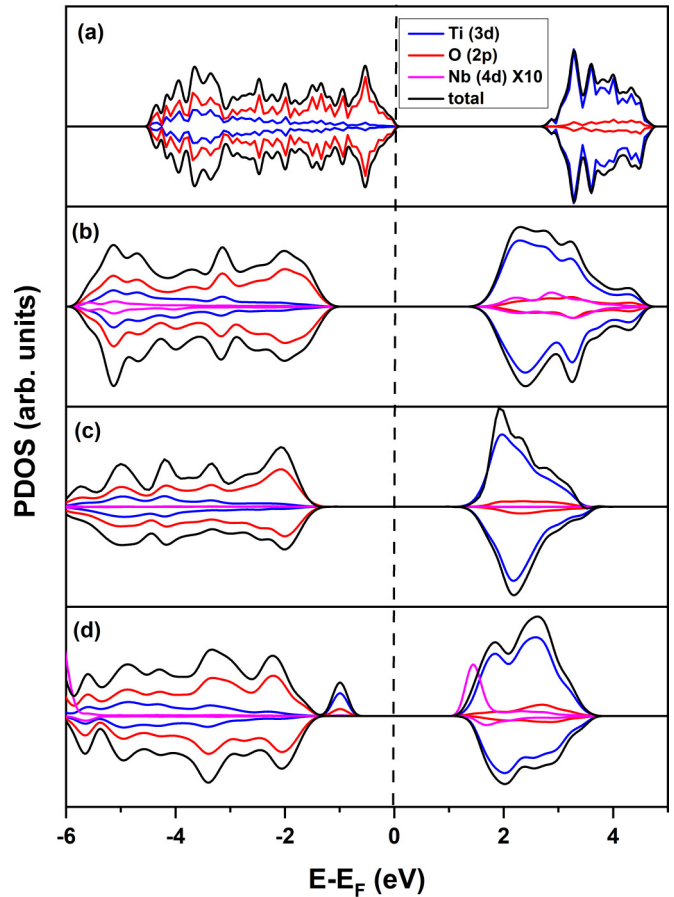
FIG. 3. PDOS of pristine and Nb-TiO_2: (a) TiO_2; (b) Nb doped at Ti_{6c}; (c) Nb-doped Ti_{5c}; and (d) Nb interstitial doped TiO_2.

Nb doping at Ti_{6c} and Ti_{5c} sites, the picture remains more or less the same, with dopant Nb 4*d* states appearing in the conduction band [see Figs. 3(b) and 3(c)]. The band gap is slightly reduced in Nb-TiO_2, which impacts the conductivity. This is consistent with the results of experimental studies of Nb-doped TiO_2 [29]. In the case of interstitial doped Nb [see Fig. 3(d)], midgap states are prominent close to Fermi energy and are primarily composed of Ti 3*d* states; Nb 4*d* states contribute to the conduction-band edge, and there is a significant reduction the band gap compared to pristine TiO_2.

B. Adsorption of O_2 and ORR intermediates

To evaluate the ORR activity of Nb-TiO_2, we examined the adsorption of O_2 and ORR intermediates on the surface. First, we looked at adsorption of O_2 on pristine TiO_2, atop a Ti atom. The initial step for ORR, which is the adsorption of O_2, plays a crucial role in the subsequent steps. The adsorption of O_2 on pristine TiO_2 is very weak (see Table II for adsorption energy), in the nature of physisorption. The gas-phase O–O bond length, which is 1.23 Å, remains unaltered after adsorption. Hence, it may be concluded that pristine TiO_2 is inactive catalytically in ORR.

For Nb-TiO_2, with Nb at Ti_{6c} and Ti_{5c} sites, the possible adsorption sites have been identified and marked as *A*, *B*, and

TABLE II. Computed values of adsorption energy of O_2, O–O, and metal–O bond lengths for pristine and Nb-doped TiO_2.

System	Site	E_{ads} (eV)	d_{O-O} (Å)	d_{M-O} (d_1, d_2) (Å)
Pristine TiO_2	Ti	−0.13	1.23	(2.93, 3.78)
Nb-TiO_2 Ti_{6c} site	A	−0.88	1.32	(2.03, 2.05)
	B	−0.90	1.32	(2.03, 2.05)
	C	−0.81	1.31	(2.04, 2.04)
Nb-TiO_2 Ti_{5c} site	A	−0.87	1.32	(2.04, 2.04)
	B (Nb)	−1.16	1.33	(2.13, 2.13)
	C	−0.80	1.32	(2.04, 2.04)
Nb-TiO_2 interstitial	A	−1.71	1.44	(1.86, 1.86)
	B	−2.57	1.45	(1.85, 1.85)
	C	−1.42	1.42	(1.89, 1.88)

C in Figs. 4(a) and 4(b). It is to be noted that in case of Ti_{5c}, the site B refers to O_2 adsorption atop of Nb atom itself.

Of these three sites on Ti_{6c} and Ti_{5c} structures, the site B is the preferred site for O_2 adsorption, with adsorption energies of −0.90 and −1.16 eV, respectively. These values indicate significant chemisorption of the O_2 molecule at these sites. The adsorption energy for all sites in the Ti_{6c} and Ti_{5c} structures are tabulated in Table II. We see that in all cases, there is chemisorption of O_2. Atop the Nb atom (B site for 5c), we see a particularly strong binding for the O_2 molecule. The O–O bond is found to be stretched from the gas-phase values by ∼ 7%. The Ti–O bond length is now shorter than in the case of pristine TiO_2, with one of the Ti–O bonds being longer than the other, owing to side-on configuration of the adsorbed O_2 molecule.

FIG. 4. Sites for O_2 and intermediates adsorption on Nb-doped TiO_2. Available distinct sites are marked A, B and C on each figure. (a) Ti_{6c}, (b) Ti_{5c}, (c) interstitial S4, and (d) O_2 adsorbed on 6c doped site, with relevant bond lengths marked. Blue, violet, and red spheres represent Ti, Nb, and oxygen, respectively. Adsorbed O_2 molecule is in dark brown.

In the case of interstitial doped TiO_2, the adsorption sites are shown in Fig. 4(c). Again, B is the preferred site, showing strong chemisorption. Additionally, the bond-length extension of O_2 at the B site is found to be 1.45 Å, which is suitable for the formation of peroxide species (which has typical bond length of ∼ 1.49 Å). Inspecting Table II, we see that in general, adsorption at the interstitial site is stronger than other sites, with O–O bonds stretched to lengths greater than 1.40 Å.

In all cases of doping, excess electrons from the d orbitals of doped TiO_2 are transferred to the $2\pi*$ orbital of O_2. From Bader charge analysis, the amount of charge transferred in Ti_{6c}, Ti_{5c}, and interstitial is 0.42, 0.46, and 0.78 e^-, respectively. This results in the elongation of the adsorbed O_2 bond length at these sites. The magnitudes of the charge transfer agree with the trends in adsorption at these sites. These excess electrons are transferred from the TiO_2 surface to the O_2 molecule, leading to the formation of a peroxide radical.

The difference charge density due to O_2 adsorption at the B site in Ti_{6c}, Ti_{5c}, and interstitial are shown in Figs. 5(a)–5(c). Figure 5(c) illustrates that the electron transfer is more significant in the case of interstitial doped TiO_2, with a doughnut-shaped electron accumulation on each O of O_2. In contrast, the electron density is much lower in the case of doping at Ti_{6c} and Ti_{5c}.

We have also optimized the configurations and calculated the binding energies of other ORR intermediates (OOH, O, OH, H, H_2O_2, and H_2O) on Nb-TiO_2 (see Supplemental Material Table S2) [57]. These calculations indicate that the most favorable adsorption site for all intermediates is the B site in Ti_{6c}, Ti_{5c}, and interstitial Nb-TiO_2. It is observed that O, OOH, and OH are strongly chemisorbed on the Ti_{5c} and interstitial sites. Weaker O and OH species adsorption generally result in higher catalytic activity. Thus, Ti_{6c} Nb-TiO_2 is expected to exhibit better catalytic activity than the Ti_{5c} and interstitial one. It is also found that H atom binds well onto the O atoms in TiO_2. These sites have either two coordinated or the three coordinated oxygens, with the two coordinated sites being preferred for H adsorption (see Supplemental Material Table S3) [57].

C. Transition-state search for ORR in Nb-TiO_2

The initial step of ORR is the chemisorption of O_2 on the electrocatalyst surface. Following this, the remaining ORR reactions may be grouped into three possible mechanistic
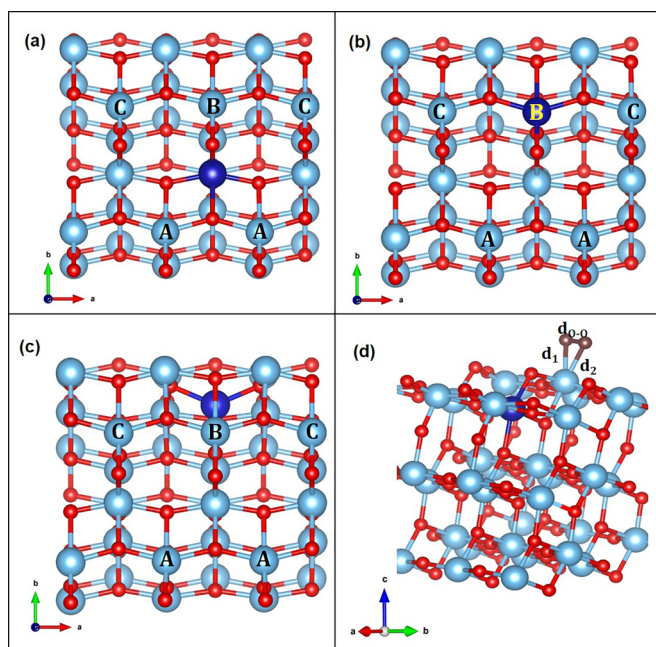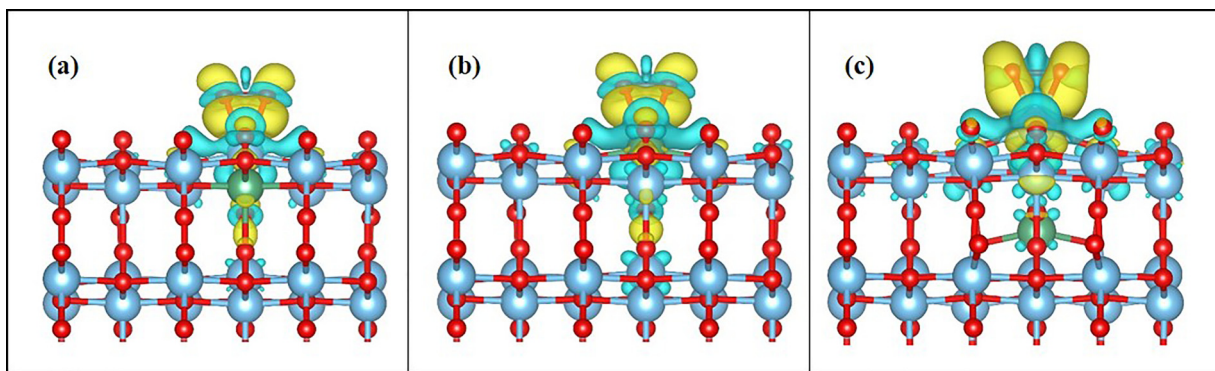
FIG. 5. Difference charge density of O_2 adsorbed at B site of Nb-TiO$_2$: (a) Ti$_{6c}$; (b) Ti$_{5c}$; and (c) interstitial (isosurface level $= 2 \times 10^{-3}$ e Å^{-3}; yellow area represents charge accumulation and blue area represents charge depletion), where blue, violet, and red spheres represent Ti, Nb, and oxygen, respectively.

pathways, namely, (i) the oxygen dissociation mechanism; (ii) the peroxyl association mechanism; and (iii) the hydrogen peroxide dissociation mechanism. A flow chart illustrating the ORR pathway is shown in Fig. 6. In general, each step involves either the scission of the O–O bond, or a series of protonation steps. The chemisorbed O_2 can undergo an O–O bond scission via a dissociative path to form *O, as shown in path (i) in Fig. 6. Alternatively, an associative path may be taken, where the chemisorbed O_2 is hydrogenated to form *OOH, which then further breaks down to form *O and *OH, in an OOH dissociation mechanism [path (ii), Fig. 6], or it can be hydrogenated to form HOOH, which then is the H_2O_2 dissociation mechanism [path (iii), Fig. 6].

We have calculated the enthalpy of reaction (ΔE) and activation energy (E_a) of all the reaction intermediates, tabulated in Table III. ΔE refers to the change in enthalpy (heat of reaction) during a particular step in any of the pathways. A positive (negative) enthalpy change indicates an endothermic (exothermic) reaction. The activation energy E_a is defined as the energy difference between the transition and initial states. The structures of the initial and final states are obtained by adsorption of the reactants and products, respectively, of the chemical reactions involving the intermediates. The optimized geometries of the initial state (IS), transition state (TS), and final state (FS) of ORR intermediates for the O–O bond scission and hydrogenation in the case of Ti$_{6c}$ Nb-TiO$_2$ are shown as an example in Fig. 7.
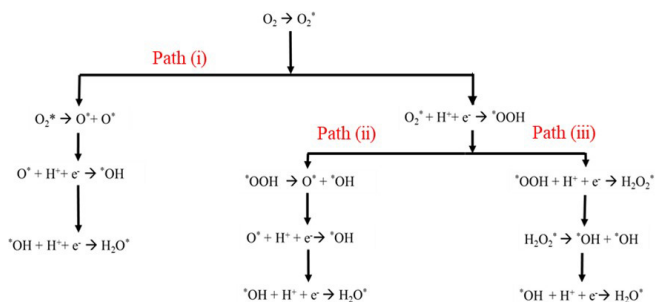
While adsorption of O_2 has been understood in detail the previous section, it is still unclear whether the adsorbed O_2 further gets dissociated or hydrogenated. The results of CI-NEB calculations indicate that the barriers for the dissociation of O_2 in Ti$_{6c}$, Ti$_{5c}$, and interstitial Nb-TiO$_2$ are too high compared to those for its hydrogenation (as seen by comparing the E_a values of the first row under dissociation and first row under hydrogenation in Table III). This is so even at the interstitial site, where the adsorption energy of O_2 is relatively higher. However, a glance at the reaction enthalpies (ΔE) shows that the dissociation pathway for interstitial doped TiO$_2$ is also favored due to the high exothermic value for the dissociation at the interstitial site. Meanwhile, in the cases of
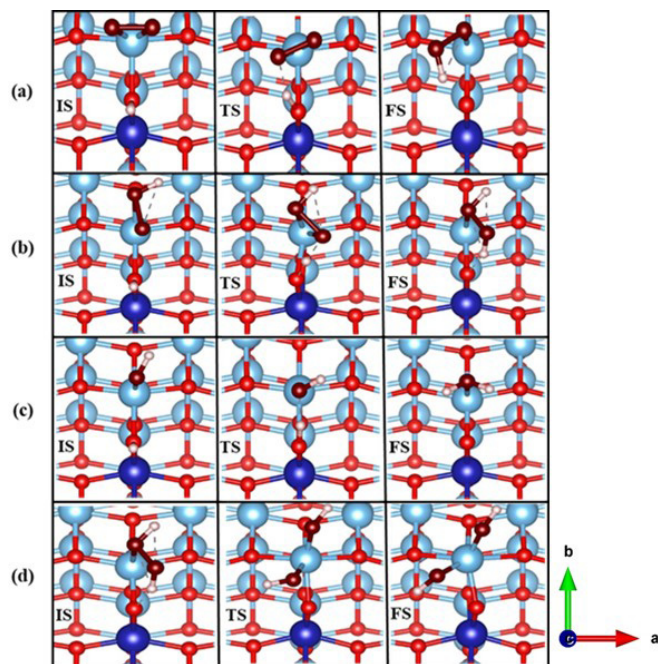

FIG. 7. Initial state (IS), transition state (TS), and final state (FS), for hydrogenation of (a) O_2, (b) OOH, (c) OH, and (d) dissociation of H_2O_2 in 6c Nb-TiO$_2$, where blue, violet, red, and white spheres represent Ti, Nb, oxygen, and hydrogen, respectively. Adsorbed O is in dark brown.

FIG. 6. Flow chart of ORR pathway showing three possible mechanisms.

TABLE III. Calculated enthalpy of reaction (ΔE) and activation energy (E_a) for various intermediate steps of ORR on Ti_{6c}, Ti_{5c}, and interstitial doped site.

Site		Ti_{6c}		Ti_{5c}		Interstitial	
	Intermediate reaction	ΔE (eV)	E_a (eV)	ΔE (eV)	E_a (eV)	ΔE (eV)	E_a (eV)
Dissociation	$O_2^* \rightarrow O^* + O^*$	+1.32	1.84	+0.60	1.94	−2.69	1.10
	$HOO^* \rightarrow O^* + HO^*$	+0.57	1.03	+0.18	0.94	−3.43	0.70
	$H_2O_2^* \rightarrow HO^* + HO^*$	−0.13	0.26	−0.35	0.24	−3.48	0.00
Hydrogenation	$O_2^* + H^* \rightarrow HOO^*$	−0.16	0.34	+0.04	0.59	−0.09	0.54
	$HO^* + H^* \rightarrow H_2O^*$	−0.46	0.29	−0.03	0.53	+0.33	0.69
	$O^* + H^* \rightarrow HO^*$	−0.60	0.33	−0.14	0.77	−0.46	0.79
	$HOO^* + H^* \rightarrow H_2O_2^*$	−0.04	0.48	+0.34	0.90		

Ti_{6c} and Ti_{5c}, the barrier values seem to encourage hydrogenation. These observations suggest that both dissociation of O_2 and hydrogenation can contribute to the ORR at room temperature.

Thus, the hydrogenation of adsorbed O_2 to form *OOH occurs at Ti_{6c}, Ti_{5c}, and interstitial sites. The intermediate species *OOH binds strongly to the Nb-TiO_2 with an adsorption energy of −2.28 eV (Ti_{6c}), −2.77 eV (Ti_{5c}), and −3.27 eV (interstitial). Following the generation of OOH, either the O–O bond scission occurs [path (ii) in Fig. 6], or hydrogenation of OOH [path (iii) in Fig. 6] takes place. The activation barrier for dissociation of *OOH is 1.03 eV (Ti_{6c}) and 0.94 eV (Ti_{5c}), and the reaction is endothermic (Table III). Compared with this, the hydrogenation of OOH is energetically favorable, with a barrier of 0.48 eV (Ti_{6c}) and 0.90 eV (Ti_{5c}).

The dissociation of H_2O_2 occurs with the scission of the O–O bond, with a barrier of 0.26 eV (Ti_{6c}) and 0.24 eV (Ti_{5c}). This barrier is lower than the values reported for Pt_3Ti (0.47 eV) [59], which is Ti-doped Pt(111) surface, or for Pt(111) surface itself (0.79 eV) [60]. This is indeed an indication that Nb-TiO_2 could be an effective substitute for Pt-based catalysts. At the interstitial site, it is found that H_2O_2 dissociates through a barrierless pathway (see Table III, third row, under dissociation). This reaction is exothermic and suggests that hydrogen peroxide dissociation occurs spontaneously following the hydrogenation of OOH. We may therefore conclude that the H_2O_2 dissociation mechanism is the favored pathway [path (iii) in Fig. 6] for ORR on Nb-TiO_2.

We have illustrated the fully relaxed geometry of IS, TS, and FS for pathway (iii), which involves hydrogenations of *O_2, *OH, *OOH, and the dissociation of H_2O_2 in case of Ti_{6c} Nb-TiO_2 in Fig. 7. We see that H_2O_2 adopts a twisted configuration, with one O-H pointing downward and the other along the slab's surface [Fig. 7(d)]. This is so for all configurations of doping investigated here. In the final state, the bond length between OH–OH is 2.48 Å (Ti_{6c}), 2.15 Å (Ti_{5c}), and 2.98 Å (interstitial), showing that H_2O_2 is completely dissociated.

The rate-determining step (RDS) is the step with the highest barrier in the proposed pathway. The final step in path (iii) is the protonation of OH. For this, the initial state consists of OH adsorbed atop a Ti in both Ti_{6c} and interstitial and atop Nb in Ti_{5c}, H on O_{2c}, and the final state is the formation of H_2O. The barrier for hydrogenation of *OH is 0.29 eV (Ti_{6c}), 0.53 eV (Ti_{5c}), and 0.69 eV (interstitial). In case of interstitial, the

desorption of OH has a high barrier due to the strong binding of OH to Nb-TiO_2, which makes the removal of OH difficult and hinders its activity. As a result, the protonation of OH is the RDS for interstitial Nb-TiO_2. For the Ti_{6c} and Ti_{5c} sites, the highest activation barrier is for the protonation of *OOH, i.e., 0.48 and 0.90 eV, respectively, and thus is the RDS. Study by Duan *et al.* demonstrated that RDS for Pt is (111) is OOH dissociation, with a 0.79-eV barrier [60]. Our results above indicate that the barrier in the RDS in the case of Ti_{6c} and interstitial doping is lower than that of pure Pt (111).

To summarize, we repeat the oft-quoted Sabatier principle, which says that an optimal catalyst interacts with the intermediates strongly enough so that the reactant can bind and react, but weakly enough so the products can easily desorb. These two acts can be correlated using the activation barrier. If the binding of the catalyst surface is too strong, it will hinder the substrate from achieving the transition state, which is reflected as a high activation energy. On the other hand, if the binding is too weak, the transition state will not stabilize, resulting again in high activation energy. Figure 8 compares activation energies for various intermediate steps. It is seen that for Nb-TiO_2, the average activation energy for various intermediates at the Ti_{6c} site is relatively low compared to Ti_{5c} and interstitial sites. Thus, the activity follows the order Ti_{6c} > interstitial > Ti_{5c}.
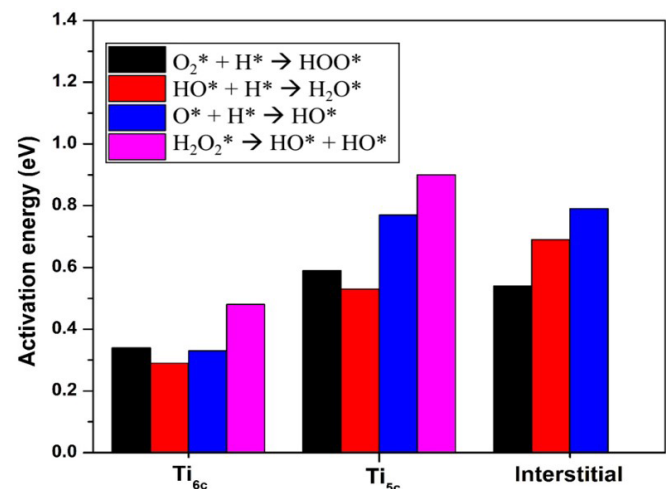
FIG. 8. Variation of activation energies of ORR intermediates for various Nb-doped TiO_2.

We conclude that Nb doping leads to enhanced ORR activity in anatase-TiO_2, enhancing its activity to compare favorably with Pt or Pt-derived materials.

D. Effect of solvation on the ORR pathway

Finally, to bring in an element of environment or medium into our model, we have considered solvation effects. Solvation effects can modify activity at sites and change activation barriers for reactions involving ORR intermediates. The chemisorbed water molecules play a crucial role in developing a more realistic model of the environment-electrode interaction, thereby bridging the gap between experiment and theory. To investigate the effect of solvation on ORR in Nb-TiO_2, we have considered water molecules coadsorbed on sites nearest to the active site, with the O atop a Ti, and H atoms pointing away from the TiO_2 slab. In a 1×3 supercell of TiO_2, there are 6 five-coordinated Ti sites. To model the solvated surface, we adsorbed 4 H_2O molecules on the surface, resulting in a coverage of 0.67 ML. This model is similar to the previous work done on pristine and defective TiO_2 anatase (101) by Tilocca and Selloni [61,62], and of Liu *et al.* [63] on Pt (111). The optimized configuration shows that the H_2O molecules are tilted at an angle of $55°$ to the surface (Fig. S5 in Supplemental Material [57]). The solvated model is also stable at room temperature, as seen through AIMD simulations performed on the solvated interstitial Nb-TiO_2, controlled by Nosé-Hoover thermostat for 5000 fs. We monitor the distance d_{Ti-O} between the O atom of the adsorbed water molecule, and the five-coordinated Ti atom at 300 K and find that d_{Ti-O} does not have any large fluctuations. This establishes the room-temperature stability of our solvation model. The time evolution of d_{Ti-O} is displayed in Fig. S6 in Supplemental Material [57]. The hydrogen of water molecule forms hydrogen bond with the bridging O_{2c}. We do not observe any $H_2O - H_2O$ bond, or dissociation of H_2O. For the pristine TiO_2 the water molecule remains close to average distance of $2.09 - 2.69$ Å from the five-coordinated Ti site. In the case of interstitial doped TiO_2 the average distance is $2.03 - 2.75$ Å.

Following this, the adsorption energy of O_2 and other ORR intermediates is calculated for all the sites (Table S4 in Supplemental Material) [57]. According to our calculations, solvation impacts adsorption strength of all intermediates, which agrees with previous studies [64,65]. This may be attributed to the formation of hydrogen bonds in case of intermediates *OH, *OOH, and *O_2H_2 with the coadsorbed H_2O molecules.

The computation of reaction barriers and enthalpy for solvated case of each site is very expensive. Hence, we have done these calculations only for the interstitial site, for which we have the largest binding energies for O_2 and intermediates. The calculated enthalpies and activation energies for various ORR intermediates in solvated interstitial doped TiO_2 are tabulated in Table IV.

Figure 9(a) shows the schematics of O_2 dissociation for the interstitial doped TiO_2, with the initial, transition, and final states. The activation energy required for the dissociation of O_2 in the solvated case is only 0.52 eV. This is a very significant reduction from the nonsolvated case, where the activation energy is 1.10 eV. O_2 dissociation with solvation

TABLE IV. Calculated enthalpy of reaction (ΔE) and activation energy (E_a) for various intermediate steps of ORR on solvated-interstitial doped site.

	Site	Interstitial (solvated)	
	Intermediate reaction	ΔE (eV)	E_a (eV)
Dissociation	$O_2^* \rightarrow O^* + O^*$	-3.01	0.52
	$HOO^* \rightarrow O^* + HO^*$	-3.29	0.09
	$H_2O_2^* \rightarrow HO^* + HO^*$	-3.83	0.10
Hydrogenation	$O_2^* + H^* \rightarrow HOO^*$	$+0.03$	0.43
	$HO^* + H^* \rightarrow H_2O^*$	-0.13	0.37
	$O^* + H^* \rightarrow HO^*$	-0.44	0.82
	$HOO^* + H^* \rightarrow H_2O_2^*$	-0.18	0.15

is shown in Fig. 9(b). In the transition state, the O–O bond distance is enlarged to 1.88 Å, and in the final state, the two O atoms are coadsorbed on Ti with an O–O distance of 2.96 Å. The greater O–O bond length in the transition state and the consequent reduction of the barrier for O_2 dissociation must be the result of hydrogen bonding in the solvated interstitial Nb-TiO_2. In the final state, we note that OH is formed, as seen clearly in Fig. 9(b). The reaction enthalpy is now more negative (-3.01 eV, Table IV) and therefore the dissociation is spontaneous. Liu and co-workers showed that the barrier for O_2 dissociation in interstitial Ti-doped TiO_2 is 1.50 eV [26], without considering solvation effects. We observe that this is quite high compared to interstitial Nb-TiO_2, with and without solvation effects.

It is interesting to note in Table IV that the enthalpy of intermediate reactions exhibits high exothermicity for dissociation compared to protonation despite a marginal increase in activation energy for O_2 dissociation, in the case of solvated interstitial doped TiO_2. Thus, the dissociation pathway is thermodynamically favorable due to its higher enthalpy of reaction than the hydrogenation. One cannot completely ignore the possibility of dissociation occurring at room temperature. The increased thermodynamic stability of the dissociated intermediates can be attributed to the stronger binding of
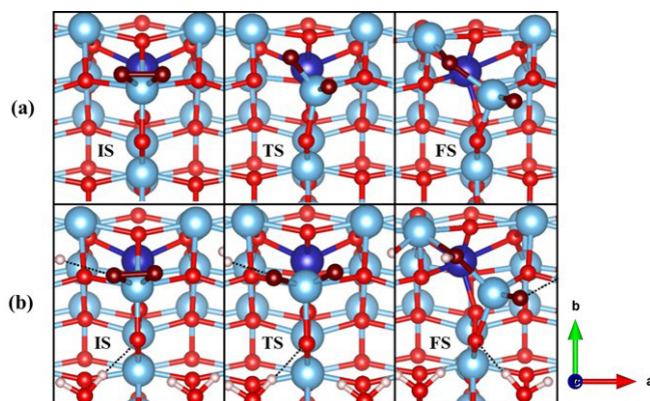

FIG. 9. O_2 dissociation in case of (a) interstitial site and (b) solvated interstitial site. Dotted lines in (b) indicate possible hydrogen bonding, where blue, violet, red, and white spheres represent Ti, Nb, oxygen, and hydrogen, respectively. Adsorbed O_2 molecule is in dark brown.

Ti-O compared to Ti-OOH. The additional stability for the dissociated intermediates in the solvated state is the result of hydrogen bonding. The optimized configurations of the solvated intermediates for the interstitial Nb-TiO$_2$ are added to the Supplemental Material [57] as Fig. S7. It is again emphasized that the hydrogenation path, which has a lower barrier, is also possible, which is validated by the small quantity of H$_2$O$_2$ formed during the reaction. This is so because H$_2$O$_2$ dissociation is also calculated to be highly exothermic (-3.83 eV). This observation is also supported by other works [66].

Solvation significantly impacts the activation energy and, therefore, the RDS of reactions. Table IV indicates that the activation energy for the protonation of O$_2$ and OH is reduced by 0.11 and 0.32 eV, respectively. Moreover, the barrier of the RDS is significantly reduced from 0.69 eV without solvation to 0.37 eV with solvation. Therefore, based on our theoretical model, we conclude that solvation strongly influences the kinetics of the ORR.

IV. CONCLUSION

In this paper, we have presented a systematic modeling study of Nb-TiO$_2$, in order to elucidate the observed ORR activity and the pathway through which it progresses. In the regime of small dopant concentration, we have considered stable configurations of Nb doped at the Ti$_{6c}$, Ti$_{5c}$, and

interstitial sites and calculated the adsorption energy of O$_2$ and intermediate species which appear in ORR. We have established that the ORR proceeds via a four-electron mechanism. The RDS of ORR activity for different sites have been determined. The order of activity of various sites is deduced to be Ti$_{6c}$ > interstitial > Ti$_{5c}$. We emphasize that high-Nb concentrations would lead to strong O$_2$ binding and inhibition of ORR. It is found that including solvation effects reduces activation barriers significantly. These conclusions are in line with recent experimental observations and establish Nb-TiO$_2$ as an excellent material for catalyzing ORR. The fact that anatase TiO$_2$ is inexpensive and nontoxic, and that Nb doping improves conductivity, additionally makes it a promising material for immediate electrochemical applications.

[1] C. Pak, S. Kang, Y. S. Choi, and H. Chang, Nanomaterials and structures for the fourth innovation of polymer electrolyte fuel cell, J. Mater. Res. **25**, 2063 (2010).

[2] Y. Feng and N. Alonso-Vante, Nonprecious metal catalysts for the molecular oxygen-reduction reaction, Phys. Status Solidi B **245**, 1792 (2008).

[3] A. Schenk, C. Grimmer, M. Perchthaler, S. Weinberger, B. Pichler, C. Heinzl, C. Scheu, F.-A. Mautner, B. Bitschnau, and V. Hacker, Platinum–cobalt catalysts for the oxygen reduction reaction in high temperature proton exchange membrane fuel cells–long term behavior under ex-situ and in-situ conditions, J. Power Sources **266**, 313 (2014).

[4] B. Fang, N. K. Chaudhari, M.-S. Kim, J. H. Kim, and J.-S. Yu, Homogeneous deposition of platinum nanoparticles on carbon black for proton exchange membrane fuel cell, J. Am. Chem. Soc. **131**, 15330 (2009).

[5] L. Huang, S. Zaman, X. Tian, Z. Wang, W. Fang, and B. Y. Xia, Advanced platinum-based oxygen reduction electrocatalysts for fuel cells, Acc. Chem. Res. **54**, 311 (2021).

[6] C. Zhang, X. Shen, Y. Pan, and Z. Peng, A review of pt-based electrocatalysts for oxygen reduction reaction, Front. Energy **11**, 268 (2017).

[7] J. Snyder, T. Fujita, M. W. Chen, and J. Erlebacher, Oxygen reduction in nanoporous metal–ionic liquid composite electrocatalysts, Nat. Mater. **9**, 904 (2010).

[8] C. Goswami, Transition metal oxide nanocatalysts for oxygen reduction reaction, Mater. Sci. Energy. Technol. **1**, 117 (2018).

[9] J. Sunarso, A. A. J. Torriero, W. Zhou, P. C. Howlett, and M. Forsyth, Oxygen reduction reaction activity of la-based

perovskite oxides in alkaline medium: A thin-film rotating ring-disk electrode study, J. Phys. Chem. C **116**, 5827 (2012).

[10] J. P. Paraknowitsch and A. Thomas, Doping carbons beyond nitrogen: an overview of advanced heteroatom doped carbons with boron, sulphur and phosphorus for energy applications, Energy Environ. Sci. **6**, 2839 (2013).

[11] L. Liao, X. Bian, J. Xiao, B. Liu, M. D. Scanlon, and H. H. Girault, Nanoporous molybdenum carbide wires as an active electrocatalyst towards the oxygen reduction reaction, Phys. Chem. Chem. Phys. **16**, 10088 (2014).

[12] Z. Jin, P. Li, and D. Xiao, Enhanced electrocatalytic performance for oxygen reduction via active interfaces of layer-by-layered titanium nitride/titanium carbonitride structures, Sci. Rep. **4**, 6712 (2014).

[13] Y. Wang, J. Li, and Z. Wei, Transition-metal-oxide-based catalysts for the oxygen reduction reaction, J. Mater. Chem. A **6**, 8194 (2018).

[14] F. Song, L. Bai, A. Moysiadou, S. Lee, C. Hu, L. Liardet, and X. Hu, Transition metal oxides as electrocatalysts for the oxygen evolution reaction in alkaline solutions: An application-inspired renaissance, J. Am. Chem. Soc. **140**, 7748 (2018).

[15] W. T. Hong, M. Risch, K. A. Stoerzinger, A. Grimaud, J. Suntivich, and Y. Shao-Horn, Toward the rational design of non-precious transition metal oxides for oxygen electrocatalysis, Energy Environ. Sci. **8**, 1404 (2015).

[16] A. L. Linsebigler, G. Lu, and J. T. Yates Jr., Photocatalysis on TiO$_2$ surfaces: Principles, mechanisms, and selected results, Chem. Rev. **95**, 735 (1995).

[17] T. L. Thompson and J. T. Yates, Surface science studies of the photoactivation of TiO$_2$ new photochemical processes, Chem. Rev. **106**, 4428 (2006).

[18] D. A. H. Hanaor and C. C. Sorrell, Review of the anatase to rutile phase transformation, J. Mater. Sci. **46**, 855 (2011).

[19] U. Aschauer, J. Chen, and A. Selloni, Peroxide and superoxide states of adsorbed O$_2$ on anatase TiO$_2$ (101) with subsurface defects, Phys. Chem. Chem. Phys. **12**, 12956 (2010).

[20] C. L. Muhich, Y. Zhou, A. M. Holder, A. W. Weimer, and C. B. Musgrave, Effect of surface deposited Pt on the photoactivity of TiO$_2$, J. Phys. Chem. C **116**, 10138 (2012).

[21] M.-C. Tsai, T.-T. Nguyen, N. G. Akalework, C.-J. Pan, J. Rick, Y.-F. Liao, W.-N. Su, and B.-J. Hwang, Interplay between molybdenum dopant and oxygen vacancies in a TiO$_2$ support enhances the oxygen reduction reaction, ACS Catal. **6**, 6551 (2016).

[22] N. R. Elezović, B. M. Babić, V. R. Radmilovic, Lj. M. Vračar, and N. V. Krstajić, Novel Pt catalyst on ruthenium doped TiO$_2$ support for oxygen reduction reaction, Appl. Catal. B **140–141**, 206 (2013).

[23] C. Chu, J. Tang, Z. Zhao, Y. Kong, and X. Shen, Fe ions-doped TiO$_2$ aerogels as catalysts of oxygen reduction reactions in alkaline solutions, Materials **15**, 8380 (2022).

[24] L. Liu, C. Li, M. Jiang, X. Li, X. Huang, Z. Wang, and Y. Jia, Mechanism of H adatoms improving the O$_2$ reduction reaction on the Zn-modified anatase TiO$_2$(101) surface studied by first principles calculation, Dalton Trans. **47**, 7541 (2018).

[25] L. Liu, Q. Liu, W. Xiao, C. Pan, and Z. Wang, O$_2$ adsorption and dissociation on an anatase (101) surface with a subsurface Ti interstitial, Phys. Chem. Chem. Phys. **18**, 4569 (2016).

[26] C. Lin, Y. Song, L. Cao, and S. Chen, Oxygen reduction catalyzed by Au-TiO$_2$ nanocomposites in alkaline media, ACS Appl. Mater. Interfaces **5**, 13305 (2013).

[27] H. Kobayashi, M. Teranishi, R. Negishi, S. Naya, and H. Tada, Reaction mechanism of the multiple-electron oxygen reduction reaction on the surfaces of gold and platinum nanoparticles loaded on titanium(iv) oxide, J. Phys. Chem. Lett. **7**, 5002 (2016).

[28] J. Li, H. Zhou, H. Zhuo, Z. Wei, G. Zhuang, X. Zhong, S. Deng, X. Li, and J. Wang, Oxygen vacancies on TiO$_2$ promoted the activity and stability of supported Pd nanoparticles for the oxygen reduction reaction, J. Mater. Chem. A **6**, 2264 (2018).

[29] Y. Furubayashi, T. Hitosugi, Y. Yamamoto, K. Inaba, G. Kinoda, Y. Hirose, T. Shimada, and T. Hasegawa, A transparent metal: Nb-doped anatase TiO$_2$, Appl. Phys. Lett. **86**, 252101 (2005).

[30] W. Yan and X. Liu, Niobium-doped TiO$_2$: Effect of an interstitial oxygen atom on the charge state of niobium, Inorg. Chem. **58**, 3090 (2019).

[31] T. Arashi, J. Seo, K. Takanabe, J. Kubota, and K. Domen, Nb-doped TiO$_2$ cathode catalysts for oxygen reduction reaction of polymer electrolyte fuel cells, Catal. Today **233**, 181 (2014).

[32] L. Chevallier, A. Bauer, S. Cavaliere, R. Hui, J. Rozière, and D. J. Jones, Mesoporous nanostructured Nb-doped titanium dioxide microsphere catalyst supports for PEM fuel cell electrodes, ACS Appl. Mater. Interfaces **4**, 1752 (2012).

[33] M. Kim, C. Kwon, K. Eom, J. Kim, and E. Cho, Electrospun Nb-doped TiO$_2$ nanofiber support for Pt nanoparticles with high electrocatalytic activity and durability, Sci. Rep. **7**, 44411 (2017).

[34] S.-Y. Huang, P. Ganesan, and B. N. Popov, Electrocatalytic activity and stability of niobium-doped titanium oxide supported platinum catalyst for polymer electrolyte membrane fuel cells, Appl. Catal. B **96**, 224 (2010).

[35] E. N. Alvar, B. Zhou, and S. H. Eichhorn, Carbon-embedded mesoporous Nb-doped TiO$_2$ nanofibers as catalyst support for the oxygen reduction reaction in PEM fuel cells, J. Mater. Chem. A **4**, 6540 (2016).

[36] Y. Sato, H. Akizuki, T. Kamiyama, and Y. Shigesato, Transparent conductive Nb-doped TiO$_2$ films deposited by direct-current magnetron sputtering using a TiO$_2$– target, Thin Solid Films **516**, 5758 (2008).

[37] S. Y. Lee, D. Numata, A. Serizawa, K. Sasaki, K. Fukushima, X. Hu, and T. Ishizaki, Systematic study of effective hydrothermal synthesis to fabricate Nb-incorporated TiO$_2$ for oxygen reduction reaction, Materials **15**, 1633 (2022).

[38] M. Yuasa, Molten salt synthesis of Nb-doped TiO$_2$ rod-like particles for use in bifunctional oxygen reduction/evolution electrodes, Ceram. Int. **48**, 14726 (2022).

[39] C. He, S. Sankarasubramanian, I. Matanovic, P. Atanassov, and V. Ramani, Understanding the oxygen reduction reaction activity and oxidative stability of Pt supported on Nb-doped TiO$_2$, ChemSusChem **12**, 3468 (2019).

[40] S. Hussain, H. Erikson, N. Kongi, A. Tarre, P. Ritslaid, A. Kikas, V. Kisand, J. Kozlova, J. Aarik, A. Tamm, V. Sammelselg, and K. Tammeveski, Platinum sputtered on Nb-doped TiO$_2$ films prepared by ALD: highly active and durable carbon-free ORR electrocatalyst, J. Electrochem. Soc. **167**, 164505 (2020).

[41] Y.-J. Wang, D. P. Wilkinson, and J. Zhang, Synthesis of conductive rutile-phased Nb$_{0.06}$Ti$_{0.94}$O$_2$ and its supported Pt electrocatalysts (Pt/Nb$_{0.06}$Ti$_{0.94}$O$_2$) for the oxygenreduction reaction, Dalton Trans. **41**, 1187 (2012).

[42] G. Kresse and J. Furthmüller, Efficient iterative schemes for ab initio total-energy calculations using a plane-wave basis set, Phys. Rev. B **54**, 11169 (1996).

[43] G. Kresse and J. Hafner, *Ab initio* molecular dynamics for liquid metals, Phys. Rev. B **47**, 558 (1993).

[44] J. P. Perdew, K. Burke, and M. Ernzerhof, Generalized gradient approximation made simple, Phys. Rev. Lett. **77**, 3865 (1996).

[45] S. Grimme, Semiempirical GGA-type density functional constructed with a long-range dispersion correction, J. Comput. Chem. **27**, 1787 (2006).

[46] S. Grimme, J. Antony, S. Ehrlich, and H. Krieg, A consistent and accurate ab initio parametrization of density functional dispersion correction (DFT-D) for the 94 elements H-Pu, J. Chem. Phys. **132**, 154104 (2010).

[47] P. E. Blöchl, Projector augmented-wave method, Phys. Rev. B **50**, 17953 (1994).

[48] L. Yan and H. Chen, Migration of holstein polarons in anatase TiO$_2$, J. Chem. Theory Comput. **10**, 4995 (2014).

[49] B. J. Morgan and G. W. Watson, A DFT+U description of oxygen vacancies at the TiO$_2$ rutile (110) surface, Surf. Sci. **601**, 5034 (2007).

[50] J. K. Burdett, T. Hughbanks, G. J. Miller, J. W. Richardson Jr., and J. V. Smith, Structural-electronic relationships in inorganic solids: powder neutron diffraction studies of the rutile and anatase polymorphs of titanium dioxide at 15 and 295 K, J. Am. Chem. Soc. **109**, 3639 (1987).

[51] G. Liu, H. G. Yang, J. Pan, Y. Q. Yang, G. Q. (Max) Lu, and H.-M. Cheng, Titanium dioxide crystals with tailored facets, Chem. Rev. **114**, 9559 (2014).

[52] J. Yu, J. Low, W. Xiao, P. Zhou, and M. Jaroniec, Enhanced photocatalytic CO_2-reduction activity of anatase TiO_2 by coexposed {001} and {101} facets, J. Am. Chem. Soc. **136**, 8839 (2014).

[53] H. J. Monkhorst and J. D. Pack, Special points for brillouin-zone integrations, Phys. Rev. B **13**, 5188 (1976).

[54] G. Henkelman, B. P. Uberuaga, and H. Jónsson, A climbing image nudged elastic band method for finding saddle points and minimum energy paths, J. Chem. Phys. **113**, 9901 (2000).

[55] R. F. W. Bader, A quantum theory of molecular structure and its applications, Chem. Rev. **91**, 893 (1991).

[56] W. Tang, E. Sanville, and G. Henkelman, A grid-based bader analysis algorithm without lattice bias, J. Phys.: Condens. Matter **21**, 084204 (2009).

[57] See Supplemental Material at http://link.aps.org/supplemental/10.1103/PhysRevMaterials.7.115801 for details on different interstitial doping sites, optimized configuration of O_2 at various interstitial sites, energy fluctuations and the structures during MD simulation, solvated surfaces, time evolution of Ti-O_W, and optimized configuration of solvated interstitial Nb-TiO_2.

[58] H. Peng, J. Li, S.-S. Li, and J.-B. Xia, First-principles study of the electronic structures and magnetic properties of 3d transition metal-doped anatase TiO_2, J. Phys.: Condens. Matter **20**, 125207 (2008).

[59] S. Kattel, Z. Duan, and G. Wang, Density functional theory study of an oxygen reduction reaction on a Pt_3Ti alloy electrocatalyst, J. Phys. Chem. C **117**, 7107 (2013).

[60] Z. Duan and G. Wang, A first principles study of oxygen reduction reaction on a Pt(111) surface modified by a subsurface transition metal M (M = Ni, Co, or Fe), Phys. Chem. Chem. Phys. **13**, 20178 (2011).

[61] A. Tilocca and A. Selloni, Structure and reactivity of water layers on defect-free and defective anatase TiO_2(101) surfaces, J. Phys. Chem. B **108**, 4743 (2004).

[62] A. Tilocca and A. Selloni, Vertical and lateral order in adsorbed water layers on anatase TiO_2 (101), Langmuir **20**, 8379 (2004).

[63] S. Liu, M. G. White, and P. Liu, Mechanism of oxygen reduction reaction on Pt(111) in alkaline solution: importance of chemisorbed water on surface, J. Phys. Chem. C **120**, 15288 (2016).

[64] J. K. Nørskov, J. Rossmeisl, A. Logadottir, L. Lindqvist, J. R. Kitchin, T. Bligaard, and H. Jónsson, Origin of the overpotential for oxygen reduction at a fuel-cell cathode, J. Phys. Chem. B **108**, 17886 (2004).

[65] J. Rossmeisl, J. K. Nørskov, C. D. Taylor, M. J. Janik, and M. Neurock, Calculated phase diagrams for the electrochemical oxidation and reduction of water over Pt(111), J. Phys. Chem. B **110**, 21833 (2006).

[66] M. Setvin, U. Aschauer, J. Hulva, T. Simschitz, B. Daniel, M. Schmid, A. Selloni, and U. Diebold, Following the reduction of oxygen on TiO_2 anatase (101) step by step, J. Am. Chem. Soc. **138**, 9565 (2016).